buildings

MDPI

Article

Numerical Analysis on Seismic Performance of Concrete-Encased CFST Columns with Two-Stage Initial Stresses

Min Zheng, Bing Tu * and Enyu Mao

School of Civil Engineering and Architecture, Guangxi University, Nanning 530004, China; 2310302096@st.gxu.edu.cn (M.Z.)
* Correspondence: tubing2018@gxu.edu.cn

Abstract

The three-stage construction of concrete-encased concrete-filled steel tubular (CE-CFST) arches introduces two-stage preloads (namely, two-stage initial stresses) within the members that critically affect their seismic behavior. This paper presents a numerical investigation into this phenomenon, employing a validated nonlinear fiber element model. The key finding is a stress-induced redistribution of internal forces that produces a dual effect: it enhances lateral capacity and ductility at low global axial compression ratios ($n < 0.5$) but impairs them at high ratios. For instance, at $n = 0.3$, gains of 3.4% in strength and 18.9% in displacement were observed. Based on parametric and theoretical analysis, a degenerate trilinear restoring force model is proposed, establishing a restoring force model for the seismic analysis of pre-stressed CE-CFST members.

Keywords: concrete-encased concrete-filled steel tubular columns; preload; seismic performance; monotonic compression-bending behavior; fiber element method; restoring force model

check for updates

Academic Editors: Yawei Fang, Tian-Qiao Liu, Junlong Yang, Zheqi Peng and Ran Deng

Received: 20 October 2025
Revised: 26 November 2025
Accepted: 1 December 2025
Published: 3 December 2025

Citation: Zheng, M.; Tu, B.; Mao, E. Numerical Analysis on Seismic Performance of Concrete-Encased CFST Columns with Two-Stage Initial Stresses. *Buildings* **2025**, *15*, 4379. https://doi.org/10.3390/buildings15234379

Copyright: © 2025 by the authors. Licensee MDPI, Basel, Switzerland. This article is an open access article distributed under the terms and conditions of the Creative Commons Attribution (CC BY) license (https://creativecommons.org/licenses/by/4.0/).

1. Introduction

The concrete-encased concrete-filled steel tubular (CE-CFST) member is a composite system characterized by its configuration: internal CFST components are surrounded by an outer reinforced concrete (RC) encasement. Representative cross-sections of this member are provided in Figure 1 [1]. This hybrid design effectively addresses several limitations inherent in conventional RC structures, such as their high self-weight, limited ductility under seismic loads, and construction complexities. Integrating the advantages of traditional CFST and RC components, CE-CFST members demonstrate enhanced mechanical properties—including high compressive strength and ductility, improved durability, exceptional fire resistance, and simplified beam-column connections [2–6]. Such merits have prompted its broad use as a primary structural component, such as in high-rise buildings, heavily loaded beam bridge piers, and large-span arch ribs [6].

The construction advantages of CE-CFST arch ribs have directly fueled their adoption in large-span bridges. This is evidenced by their use in 11 of the world's 30 longest concrete arch bridges, including the record-setting Tian'e Longtan Bridge completed in 2024. The construction process, illustrated in Figure 2, comprises three sequential stages [7]: (1) the erection of hollow steel tubes, (2) the filling of these tubes with in-tube concrete to form the CFST component, and (3) the casting of the surrounding RC encasement. This method offers significant on-site benefits, primarily by reducing the hoisting weight—as only the hollow steel tubes need to be lifted—and minimizing formwork requirements.

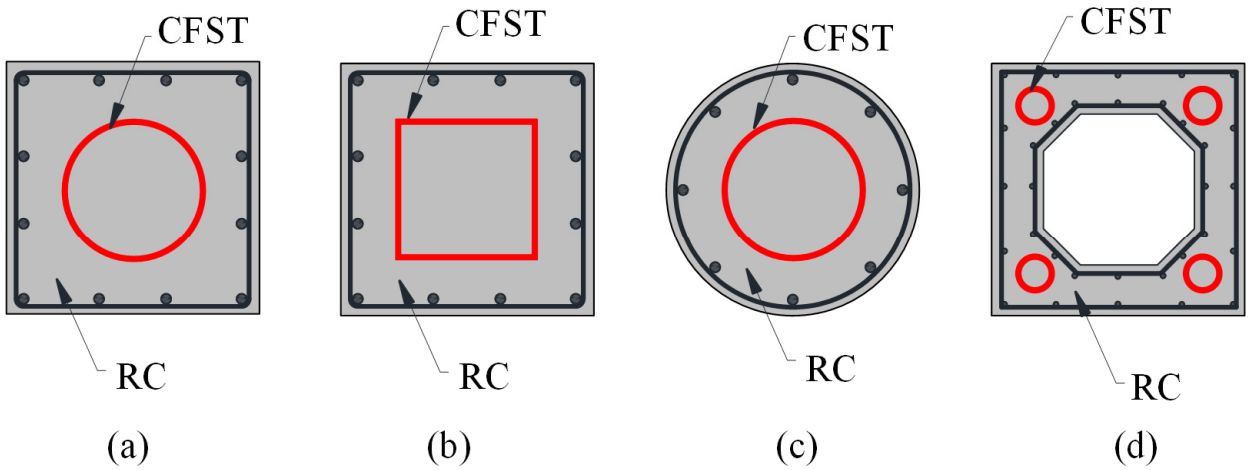


Figure 1. Representative cross-sections of the CE-CFST column. (**a**) Circular steel tube core and square concrete encasement; (**b**) Square steel tube core and square concrete encasement; (**c**) circular steel tube core and circular concrete encasement; (**d**) Multiple circular cores and voided square concrete-encased.

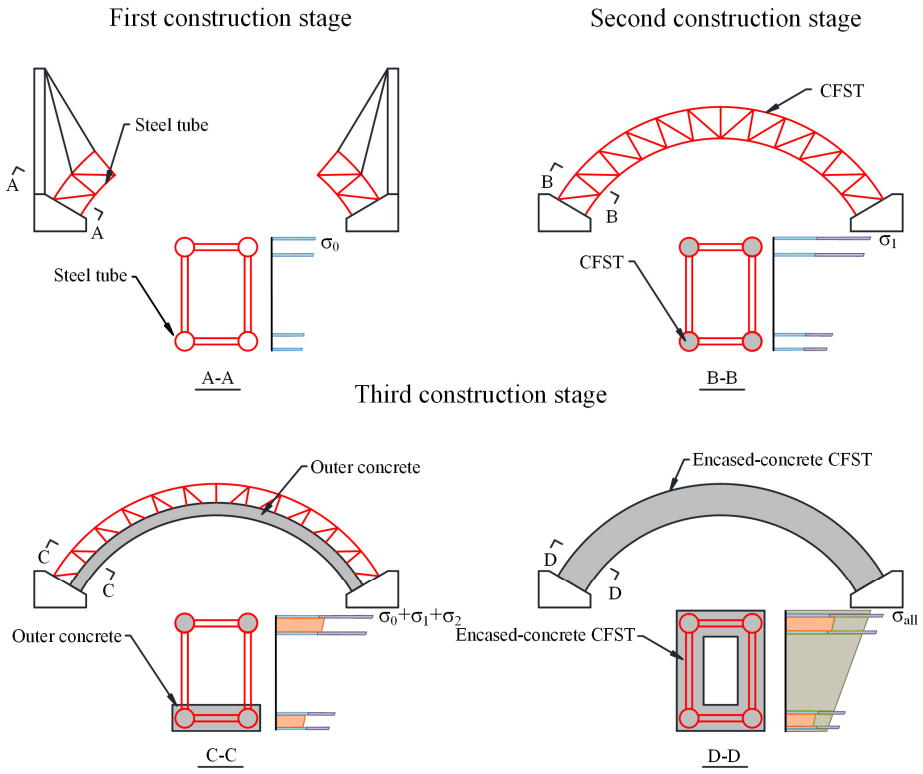


Figure 2. Construction procedure of the CE-CFST arch rib.

However, this highly efficient method introduces non-negligible two-stage preload (namely, two-stage initial stresses) to such structures. These develop sequentially: the first stage from the self-weight of the steel tube and in-tube concrete, and the second from the outer concrete encasement. A critical difference in arch ribs is that these stress-inducing loads act vertically against the curved axis, amplifying the stress levels. This is exemplified by the Tian'e Longtan Bridge [8], where preloads peaked at 270 MPa (steel tube) and 25 MPa (in-tube concrete), corresponding to notably high ratios of 0.76 and 0.72, respectively.

Obviously, the two-stage preloads in CE-CFST arch ribs lead to substantial differences in stress states under post-construction loads compared with those in conventionally cast-in-place integral members. Consequently, it is essential to examine the mechanical and

seismic performance of CE-CFST arch ribs considering these two-stage preloads. Moreover, CE-CFST arch ribs are subjected mainly to combined compression and bending, similar to eccentrically loaded straight columns. The equivalent beam-column method is therefore frequently employed to evaluate arch structure capacity, leveraging this fundamental similarity [9–12]. Therefore, the seismic performance of phased-constructed CE-CFST arch ribs can be investigated using corresponding CE-CFST columns incorporating two-stage preloads.

To date, numerous studies have examined the seismic performance of integrally formed CE-CFST columns. These investigations have comprehensively assessed specific performance metrics such as failure modes, hysteretic behavior, displacement ductility, energy dissipation, sectional strain distribution, and load-bearing capacity under monotonic and cyclic lateral loading. Existing seismic studies on CE-CFST columns have extensively covered conventional parameters like axial compression ratio, material strengths (in-tube concrete, encased concrete, and steel tube), stirrup ratio, and diameter-to-thickness ratio [2,13,14]. Beyond these, the role of preloads has been separately investigated. For the second-stage preload, simulated by preloading the CFST component, research by Li et al. [15,16] and Huang et al. [17,18] suggests a beneficial effect, enhancing ductility and seismic performance, which led to the proposed predictive formulas. In contrast, studies on the first-stage preload within the steel tube, such as those by Yu et al. [19], report a detrimental impact, reducing initial stiffness and lateral load-bearing capacity. The fundamental limitation of these prior works is their isolated consideration of either the first- or second-stage preload. This approach fails to capture the sequential construction process where the first-stage preload in the steel tube precedes and interacts with the second-stage stress applied to the composite CFST. Consequently, the coupled effect of these two-stage preloads remains unquantified, rendering existing models inadequate for representing the true preload state in CE-CFST arch ribs. These two-stage preloads result in a coupled stress history and a distinct internal force distribution that cannot be simply superimposed by two separate single-stage analyses. Consequently, the seismic performance under the combined two-stage preload condition is anticipated to be fundamentally different from that predicted by existing single-stage models. Given this pronounced gap between the simplified single-stage models in existing literature and the actual two-stage stress history in practice, there is an urgent need to develop a new analytical framework that can explicitly account for the coupled effects of two-stage preloads. However, the combined mechanical effect of these preloads remains unexamined in the existing literature.

The monotonic compression-bending test, a fundamental seismic assessment method in seismic evaluation of CE-CFST columns, is characterized by the application of a constant axial load while the column is simultaneously subjected to a monotonically increasing lateral load. On the one hand, it reveals the plastic evolution and ductility reserves of the composite members under static loading, providing insight into their deformation capacity during seismic events. On the other hand, the material's constitutive relationships and failure modes established through monotonic loading provide a foundational basis for further modeling seismic performance.

Simultaneously, a restoring force model is essential to capture the stiffness degradation, strength attenuation, and energy dissipation of CE-CFST columns with two-stage preloads under seismic loads. Cai et al. [20] and Ke et al. [21] experimentally developed skeleton curves and restoring force models for CFST and high-strength CE-CFST columns. But no model exists for CE-CFST columns subjected to the two-stage initial preloads. Currently, restoring force models for RC and steel-concrete composite members are generally categorized into two types [22]: curve-type models, consisting of curves and straight lines, and polyline-type models, composed of multiple straight-line segments. The fundamental

difference lies in their computational behavior: in curve-type models, the stiffness changes at every iteration step, leading to high computational cost, whereas polyline-type models, with fewer parameters and fixed segment stiffness, significantly reduce computational effort [23]. Although curve-type models can better capture specific response nuances, their complexity limits widespread use. Therefore, the polyline-type restoring force model is adopted in this study.

This study examines the combined influence of the two-stage preloads (acting on the steel tube and in-tube concrete) on the seismic performance of CE-CFST columns. Accordingly, a generalized fiber element method was proposed to predict their monotonic compression-bending behavior, explicitly incorporating these preloads. In contrast to existing models that are limited to single-stage stress conditions, the proposed model explicitly simulates the sequential application of preloads and their coupled effect on the composite section. Subsequently, a systematic parametric study was then performed using this method to evaluate the full-range structural response under combined axial-sustained and lateral-monotonic loading, across different preload combinations. The extent of this influence, and the mechanisms of the preloads on compression-bending behavior, were systematically elucidated. Following this, the key parameters controlling preload effects were identified through a parametric study. Guided by this parametric investigation and theoretical analysis, a restoring force model that accounts for two-stage preloads was subsequently developed for CE-CFST columns. This model can serve as a foundational constitutive relationship for the seismic design of CE-CFST structures.

2. Fiber Element Method for Analysis of Monotonic Compression-Bending Behavior

2.1. Fundamentals and Procedures of the Fiber Element Method

This study investigates a CE-CFST column characterized by a hybrid cross-section, integrating a square outer RC encasement with a single circular inner CFST; see Figure 1a. A baseline member was designed following code provisions and engineering practice, as detailed in Figure 3. The column measures 900 mm in total length, with a 300 × 300 mm outer RC section and a 168 mm-diameter inner steel tube. Longitudinal reinforcement comprises four 12 mm-diameter bars on each face, confined by 6 mm-diameter stirrups spaced at 60 mm centers. The specified concrete grades were C70 for the core and C50 for the encased concrete, conforming to the Chinese code [24]. The steel tube exhibits a yield strength of 345 MPa, while both longitudinal and transverse reinforcement have a yield strength of 335 MPa. Furthermore, the axial compression ratio is set to 0.3, a value that typically corresponds to the maximum ultimate bending moment capacity of such columns, as defined by Equation (1) [25]. The complete loading sequence applied to the column is depicted in Figure 4.

$$n = \frac{N}{f_{cu,out}A_{co} + f_{cu,core}A_{ci}(1 + 1.8\xi)} \tag{1}$$

$$\xi = \frac{A_s f_y}{A_{ci} f_{cu,core}} \tag{2}$$

where N represents the total axial compressive load, including the loads causing the two-stage preloads; $f_{cu,out}$ and $f_{cu,\mathrm{core}}$ represent the axial compressive strength of the encased concrete and in-tube concrete, respectively; A_{co} and A_{ci} represent the area of the encased concrete and in-tube concrete, respectively; f_y and A_s represent the steel tubular yield strength and area, respectively; and ξ represents the confinement coefficient of the inner CFST.

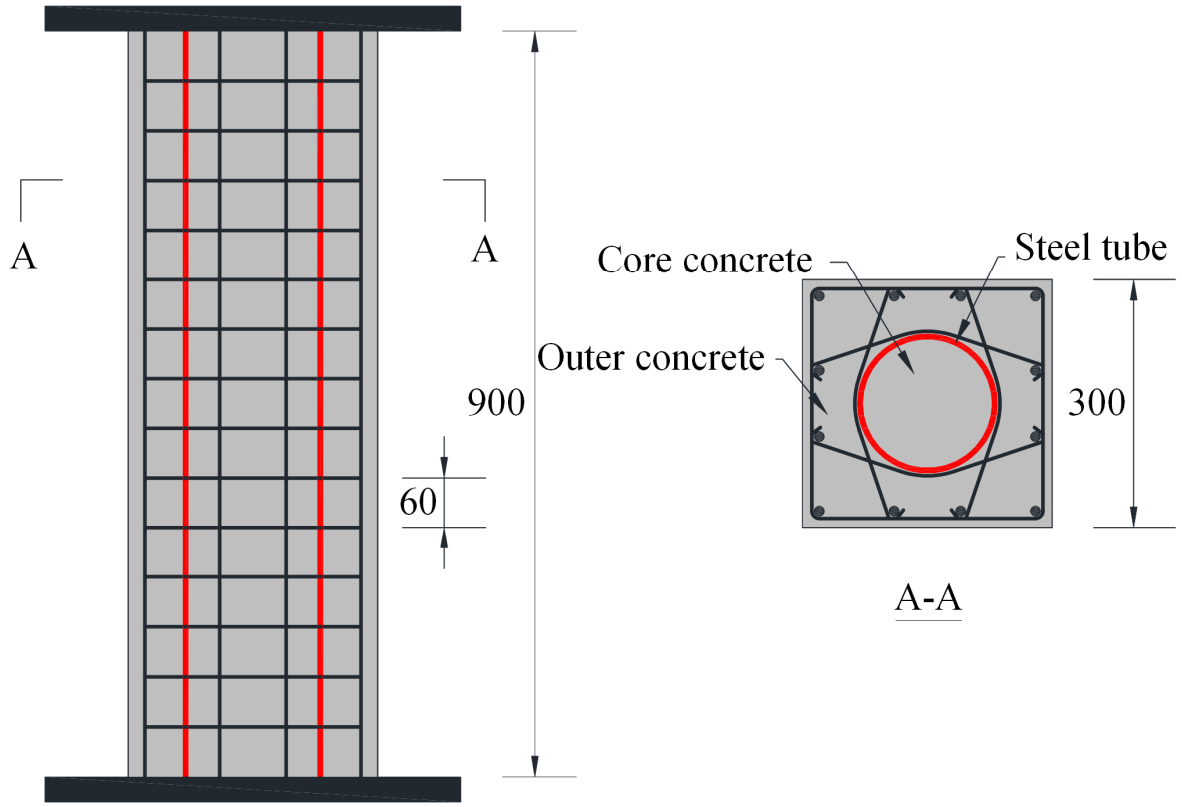


Figure 3. Configuration and dimensions of the baseline member (unit: mm).

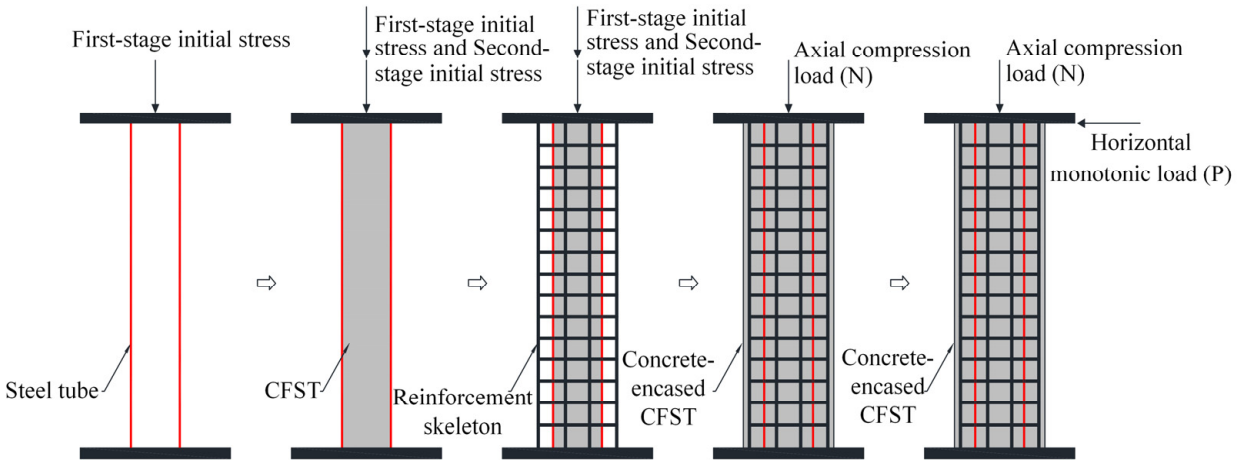


Figure 4. Total loading sequence for the baseline member.

To isolate the individual effects of the first- and second-stage preloads, a preload coefficient was defined for both the steel tube and the in-tube concrete, conceptually treating these stresses as pre-stress. The coefficient for the in-tube concrete is directly determined by that of the steel tube from the second stage. Consequently, the latter coefficient is utilized to characterize both materials, in accordance with the computational forms provided in Equations (3) and (4).

$$\beta_s = \frac{\sigma_1 + \sigma_2}{f_y} \tag{3}$$

$$\beta_c = \frac{\sigma_2}{f_y} \tag{4}$$

where β_s and β_c represent the preload coefficients for the steel tube and in-tube concrete, respectively, and σ_1 and σ_2 represent the steel tubular stress values after applying first-stage preload and second-stage preload, respectively.

The fiber element method was selected for this study due to its optimal balance between computational accuracy and efficiency. The analytical model was developed based on the following key assumptions:

1. Uniform distribution of preloads: The preloads are uniform throughout the cross-sections of the steel tube and the in-tube concrete.
2. Plane section assumption: Cross-sections that are plane before deformation remain plane after deformation. Accordingly, the increments of normal strain vary linearly over the cross-section height.
3. Negligible shear deformation: Shear deformation is disregarded in the analysis.
4. No interfacial slip: Full composite action is maintained at the steel-concrete interface, precluding any interfacial slip.
5. Linear curvature distribution: The sectional curvature is postulated to vary linearly along the column height H, as schematically represented in Figure 5. The lateral displacement (Δ) at the column top is consequently governed by the curvature ($\varnothing$) at the critical bottom section through the following expression:

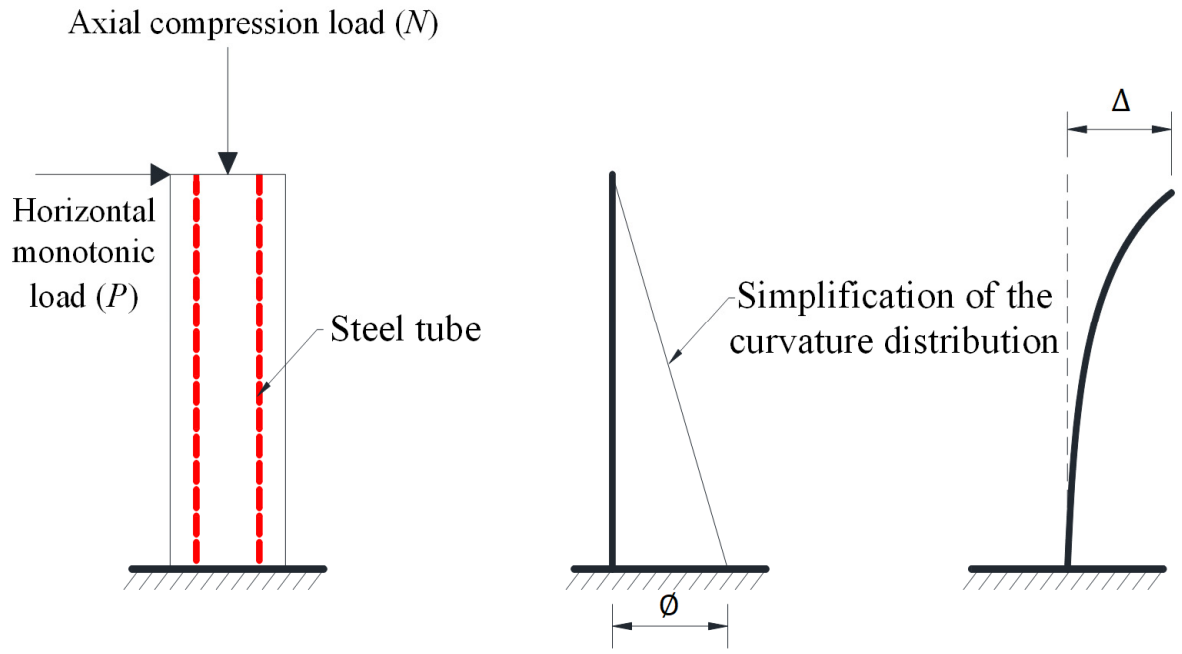


Figure 5. Schematic diagram of the computational principle.

$$\Delta = \frac{1}{3}\phi H^2 \tag{5}$$

The fiber element method, following the nonlinear computational algorithm for beam-column members, simulates the full-range monotonic compression-bending response of CE-CFST columns through an incremental iterative process, as detailed in Figure 6.

2.2. Constitutive Relationships of Materials

The fiber element method computes the mechanical response by first deriving fiber strains from the plane section assumption and then converting them to stresses through material constitutive relationships. Therefore, computational accuracy for this method necessitates precise constitutive models. The load-bearing materials in CE-CFST columns in

the longitudinal direction are categorized as follows: in-tube concrete, stirrup-confined encased concrete, unconfined cover concrete, steel tube, and longitudinal reinforcement bars.

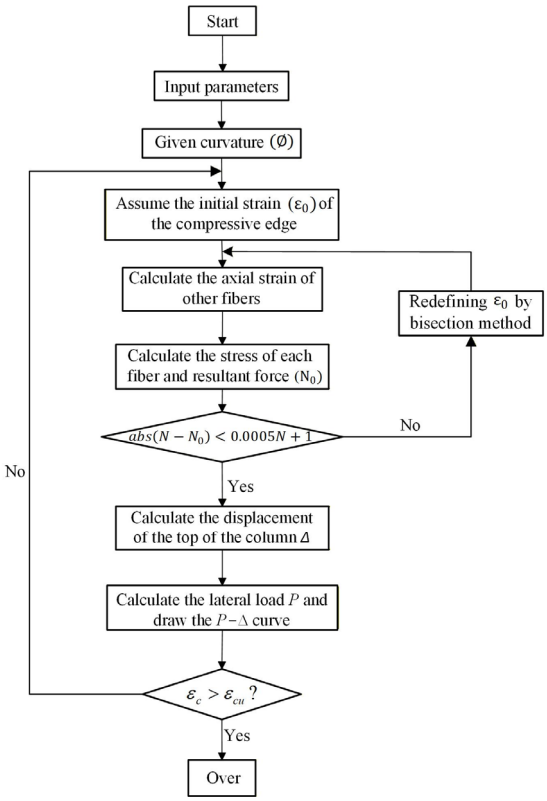
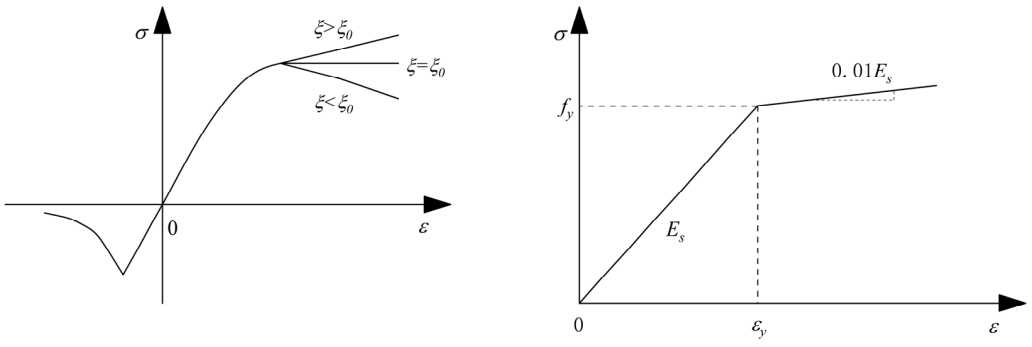


Figure 6. Fiber element method workflow.

2.2.1. Concrete

The concrete in CE-CFST columns is stratified into three types according to confinement conditions: in-tube concrete, stirrup-confined encased concrete, and unconfined cover concrete, each assigned a specific constitutive model. The constitutive behavior of the in-tube concrete, accounting for the steel tubular confining effect, was governed by the model from Han et al. [26] (Figure 7a). Meanwhile, the constitutive relationships for the stirrup-confined concrete and unconfined cover concrete were both defined in Chinese code [27]. All three types utilize the same tensile stress–strain relationship established by Shen et al. [28].



(**a**) (**b**)

Figure 7. Constitutive relationships. (**a**) In-tube concrete; (**b**) steel.

2.2.2. Steel

The constitutive model of both the longitudinal reinforcement bars and steel tube is characterized by a bilinear elastic-plastic model [26], as defined in Equation (6) and illustrated in Figure 7b.

$$\begin{cases} \sigma = E_s \times \varepsilon & \varepsilon \le \varepsilon_y \\ \sigma = f_y + 0.01E_s(\varepsilon - \varepsilon_y) & \varepsilon_y \le \varepsilon \end{cases} \quad (6)$$

where E_s, and ε_y represent the elastic modulus and yield strain of the steel tube and the longitudinal reinforcement bars, respectively.

2.3. Validation of the Proposed Fiber Element Method

To address the lack of direct experimental data on CE-CFST columns with combined two-stage preloads, the present model was validated against existing research. The verification encompassed three critical scenarios: CE-CFST columns without preload [2,14], CFST columns with first-stage preload [19], and CE-CFST columns under second-stage preload [16]. Table 1 summarizes the key specimen parameters and experimental results. Here, P_{exp} is the average ultimate lateral load-bearing capacity from experimental tests in both positive and negative loading directions, and P_{fib} is the corresponding value predicted by the fiber model. The comparison yields a mean P_{fib}/P_{exp} ratio of 0.96 with a standard deviation of 0.113, indicating close agreement between numerical predictions and experimental measurements.

Table 1. Experimental ultimate strength and predicted ultimate strength of CE-CFST columns.

Specimen Type	Specimen	D (mm) × t (mm)	B (mm)	f_y (MPa)	$f_{c,out}/f_{c,core}$ (MPa)	N (KN)	Stirrups	β_1	β_2	P_{exp} (kN)	P_{fib} (kN)	P_{fib}/P_{exp}
CE-CFST column without preload	CCS1 [14]	168 × 5.76	300	354	53.0/72.2	1038	6@63	-	-	268.2	233.4	0.87
	CCS2	168 × 5.76	300	354	53.0/72.2	1025	6@80	-	-	266.5	233.6	0.88
	CCS3	168 × 5.76	300	354	54.0/67.3	1377	6@47	-	-	242.7	240.0	0.99
	CCS4	168 × 5.76	300	354	54.0/67.3	1365	6@60	-	-	233.5	239.0	1.02
	CCS5	168 × 5.76	300	354	58.3/68.7	1708	8@65	-	-	252.2	248.9	0.99
	CCS6	168 × 5.76	300	354	58.3/68.7	1697	6@65	-	-	249.7	246.4	0.99
	CCS7	168 × 5.76	300	354	59.4/74.1	2045	8@56	-	-	242.2	250.7	1.04
	CCS8	168 × 5.76	300	354	59.4/74.1	2040	6@50	-	-	260.7	247.5	0.95
	CCS9	168 × 5.76	300	354	57.1/73.1	2201	8@48	-	-	262.7	245.9	0.94
	CCS10	168 × 5.76	300	354	57.1/73.1	2188	6@44	-	-	280.7	241.5	0.86
CE-CFST column without preload	SC1 [2]	60 × 2	150	353	33.6/52.4	0	6@100	-	-	42.6	46.5	1.09
	SC2	60 × 2	150	353	33.6/52.4	282	6@100	-	-	55.8	50.8	0.91
	SC3	60 × 2	150	353	33.6/52.4	564	6@100	-	-	61.8	42.6	0.69
CFST column with first-stage preload	M1 [19]	219 × 4	-	316	-/22.3	900	-	0	-	76	66.3	0.87
	M2	219 × 4	-	316	-/22.3	900	-	0.4	-	55	64.7	1.18
	M3	219 × 4	-	316	-/22.3	900	-	0.6	-	72	63.9	0.89
CE-CFST column with second-stage preload	S-1 [16]	84.4 × 2.5	202 × 205	274	42.1/85.5	670	5@50	-	0.3	97	115.2	1.19
	S-2	84.4 × 2.5	200	274	53.8/85.5	870	5@50	-	0.31	146	145.8	1.00
	S-3	84.4 × 2.5	200	274	53.2/85.5	1063	5@50	-	0.28	166	142.8	0.86
	S-4	89 × 5	200	274	72.0/85.5	1081	5@50	-	0.3	169	164.2	0.97

Note. D and t represent the steel tubular outer diameter and wall thickness, respectively; B represents the cross-sectional side length of the CE-CFST column; $f_{c,out}$ and $f_{c,core}$ are the cylinder compressive strengths of the encased concrete and the in-tube concrete, respectively; and N represents the axial compression force.

Furthermore, given that the load–displacement curves under monotonic lateral loading correspond well to the skeleton curves under cyclic loading for RC or steel-concrete composite columns [26], the experimentally measured skeleton curves from CE-CFST quasi-static test (Qian et al.) [14] were compared with the monotonic load–displacement curves

predicted by the fiber model. As shown in Figure 8, the numerical predictions demonstrate strong agreement with the experimental measurements.

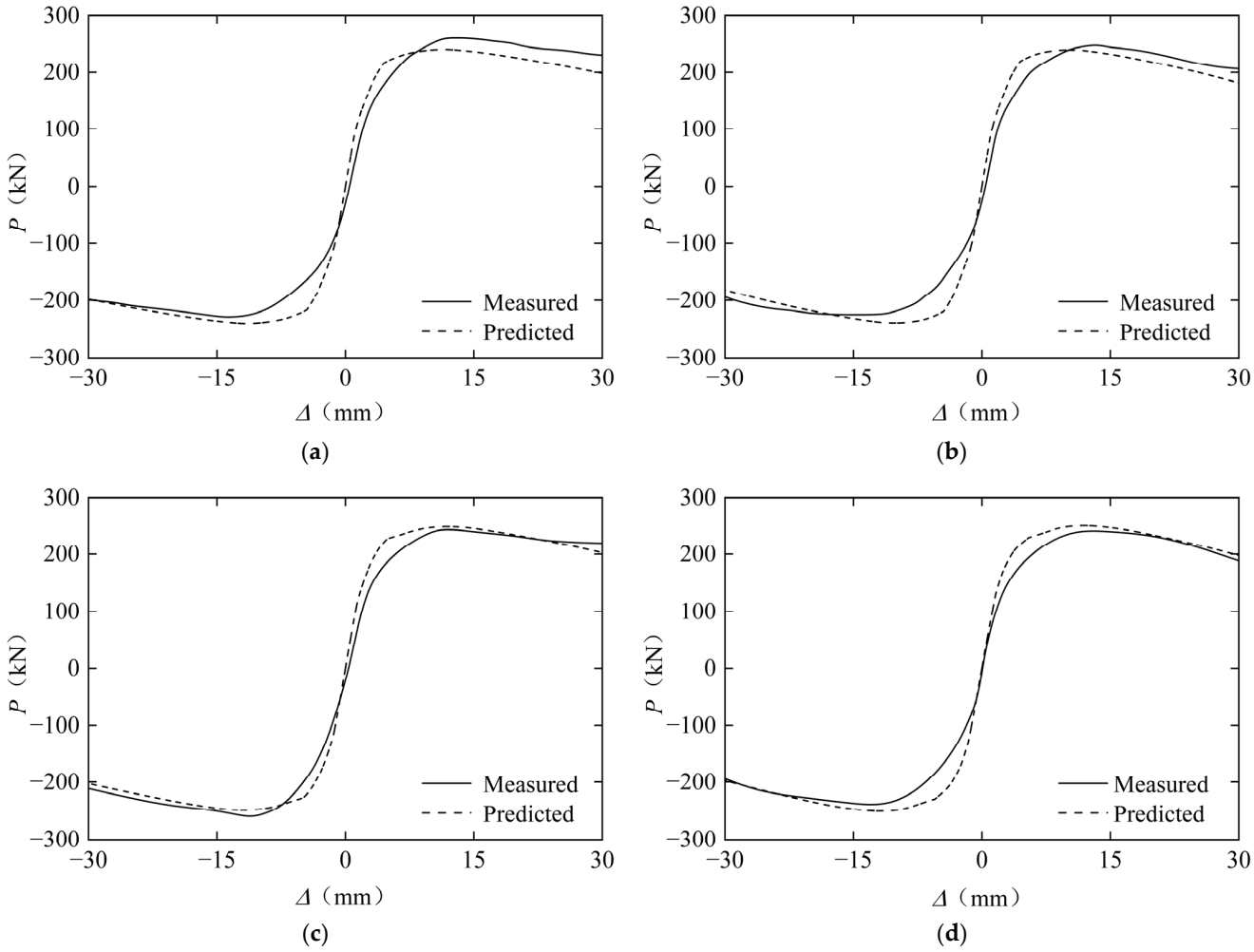


Figure 8. Measured and predicted monotonic loading load–displacement curves. (**a**) Specimen CCS3; (**b**) Specimen CCS4; (**c**) Specimen CCS5; (**d**) Specimen CCS7.

The verification study demonstrates that the developed fiber element method accurately captures the monotonic compression-bending behavior of the members. This outcome establishes the method as a robust tool for systematically investigating the influence of two-stage preloads on CE-CFST column performance.

3. Effects of Two-Stage Preloads on Monotonic Compression-Bending Behavior

3.1. Effects of Two-Stage Preloads on Lateral Load–Displacement Relationship

The lateral load–displacement relationship serves as a critical indicator for assessing the complete structural behavior of CE-CFST columns subjected to lateral load. Accordingly, an in-depth analysis of this relationship is conducted first. Figure 9 compares the lateral load–displacement curves obtained under various preload combinations. The parameters of these columns correspond to those of the baseline member presented in Figure 3.

Both the steel tube and in-tube concrete preloads demonstrate negligible effects on the load–displacement curves. A key observation is that during the initial loading phase, the curves for specimens with different preloads nearly coincide, indicating a negligible effect during this stage. With further loading, however, the structural response is characterized

by reduced stiffness, lowered ultimate lateral resistance, and increased displacement at peak load due to preloads. These effects become more pronounced with increasing preload. For example, as shown in Figure 9a, when β_c = 0, the ultimate lateral load-bearing capacity with $\beta_s = 0.2$, 0.4, and 0.6 decreases by 1.0%, 2.2%, and 3.4%, respectively, compared to the case with $\beta_s = 0$, while the corresponding displacements increase by 6.41%, 11.7%, and 18.9%. Similarly, for specimens with β_c = 0.2, 0.4, and 0.6 (Figure 9c), the ultimate lateral load-bearing capacity decreases by 0.3%, 0.9%, and 1.7%, respectively, with corresponding displacement increments of 2.3%, 7.5%, and 14.7%, relative to the case with β_c = 0. These results demonstrate that preloads significantly improve ductility, as observed in the converging post-peak load–displacement curves. This enhanced energy dissipation capacity is vital for seismic safety, transforming the design strategy for CE-CFST columns from compensating for initial stresses to actively leveraging them.

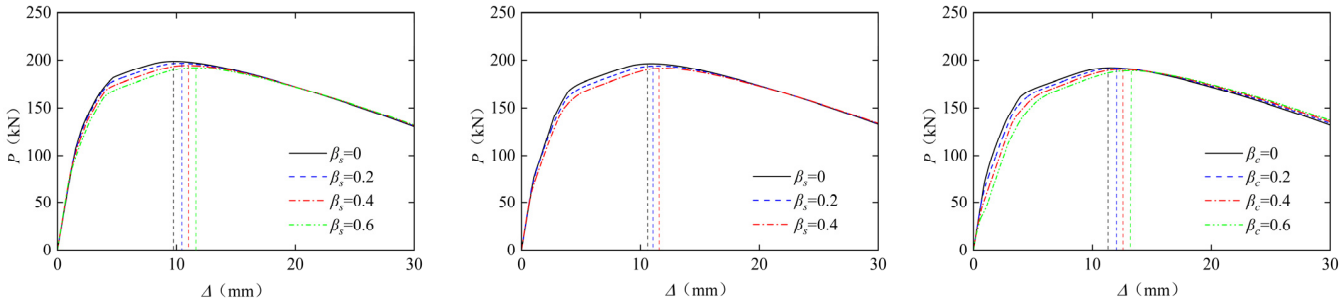


Figure 9. Load–displacement curves under varying preload combinations: (**a**) $\beta_c = 0$; (**b**) $\beta_c = 0.2$; (**c**) $\beta_s = 0.6$.

3.2. Effects of Two-Stage Preloads on Load-Bearing Mechanism

This study employed the fiber element method to disaggregate and assess the individual axial and lateral load contributions within CE-CFST columns, thereby clarifying their load-bearing mechanism under two-stage preloads. Figure 10 illustrates the evolution of the encased concrete's contribution ratio to both axial and lateral load resistances under various preload combinations.

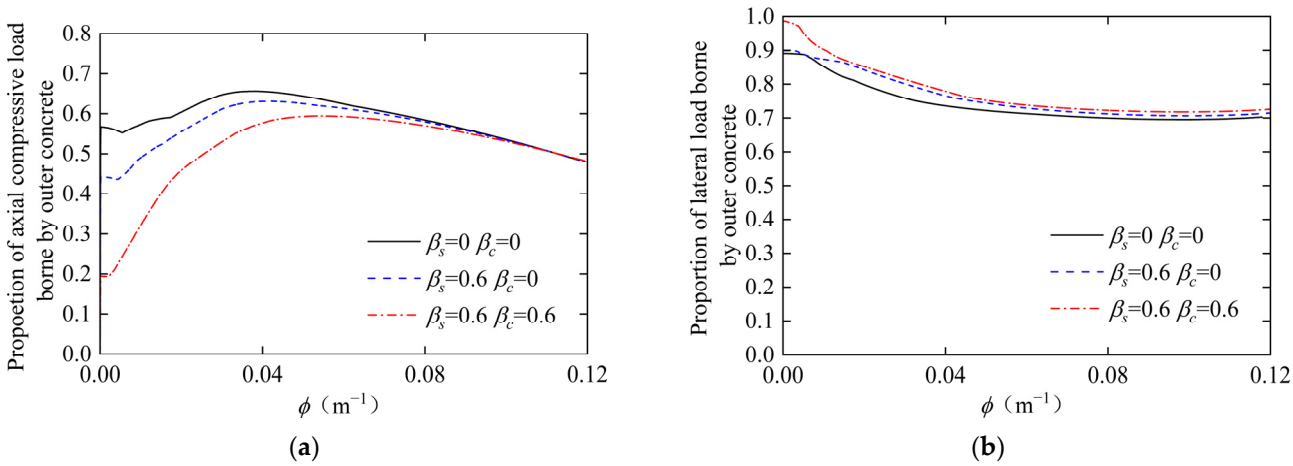


Figure 10. Curves of load proportion carried by encased concrete with curvature under varying preload combinations: (**a**) Axial load; (**b**) lateral load.

Figure 10a demonstrates consistent trends in the axial load proportion borne by the encased concrete across various preload states. This proportion initially rises but later declines with increasing lateral load. The structural response can be explained as follows:

the initial application of lateral load causes the sectional neutral axis to move, which redistributes more axial force to the peripherally located encased concrete. After the attainment of the peak lateral load, the axial force progressively redistributes toward the inner CFST due to ongoing plasticity and concrete cracking. The presence of preloads continuously influences this load distribution mechanism.

The impact of preloads is immediately evident in the reduced load contribution of the encased concrete. At the onset of lateral loading, its contribution ratio falls to 20% (with preloads) from a baseline of 57% (without preloads). Although this ratio later rises to a peak of 56% in the presence of preloads, it remains notably lower than the 66% peak observed in the stress-free column. This difference arises mainly because the preloads alter the strain distribution under axial loading, which accentuates disparities in stress development between the core and encased concrete during flexural loading, thereby leading to distinct patterns of axial load redistribution. Furthermore, the encased concrete in CE-CFST columns typically exhibits lower ductility under combined compression and bending than the inner CFST core of such columns. This issue is mitigated by the introduction of preloads, which shift the axial load away from the encased concrete and thereby reduce its axial compression ratio. This mechanism leads to improved ductility of CE-CFST columns under the influence of preloads, demonstrated in Section 3.1. By the final loading stage, the axial load contribution ratio of the encased concrete stabilizes at approximately 48% under all preload conditions.

Figure 10b indicates that the encased concrete generally makes a substantial contribution to the lateral load resistance in CE-CFST columns. This occurs primarily because the centrally located CFST component of the cross-section provides limited resistance to bending. Moreover, the lateral load contribution ratio of the encased concrete exhibits a consistent evolutionary pattern under all preload conditions: during the initial loading stage, it accounts for more than 90% of the total lateral resistance; as loading continues, this proportion gradually decreases and eventually stabilizes at approximately 70%.

To elucidate this behavior, the lateral load contributions between the encased concrete and the inner CFST component under different preload combinations were examined, as plotted in Figure 11. The results illustrate that preloads decrease the lateral load contribution of both components before the peak load is reached. This is attributed to the way preloads alter the actual axial compression ratios: they lower the ratio for the encased concrete but increase it for the inner CFST. Consequently, the lateral capacity of both components diminishes when subjected to very high or very low axial compression ratios. Nevertheless, the proportional reductions in lateral load sustained by the encased concrete and the CFST are similar, leading to a relatively constant load contribution ratio between the two components. In the post-peak stage, the lateral load contributions from both components stabilize at comparable levels, regardless of the preload conditions.

In conclusion, the initial loading stage is particularly critical for CE-CFST columns, as it is where the preloads exert their most substantial influence on the subsequent compression-bending behavior. As deformation progresses, a convergence in the axial and lateral load distribution among the components occurs. This progressive load redistribution is the underlying mechanism that drives the post-peak load–displacement curves toward alignment, as evidenced in Figure 9.

3.3. Effects of Two-Stage Preloads on Compression Zone Depth

In the seismic design of concrete structures, the compression zone depth is a critical indicator. It refers to the vertical distance between the neutral axis and the extreme compression fiber, marking the effective depth of concrete engaged in carrying compres-

sion. Figure 12 compares the evolution of the compression zone depth with the sectional curvature of CE-CFST columns under various preload combinations.

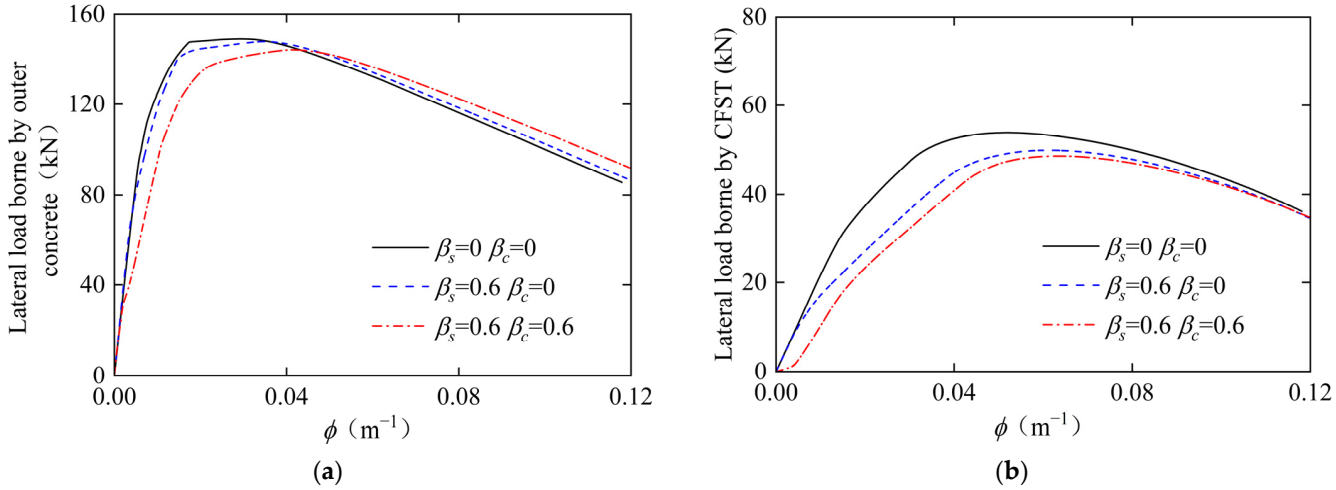


Figure 11. Curves of lateral load carried by different components with curvature under varying preload combinations: (**a**) Encased concrete; (**b**) inner CFST.

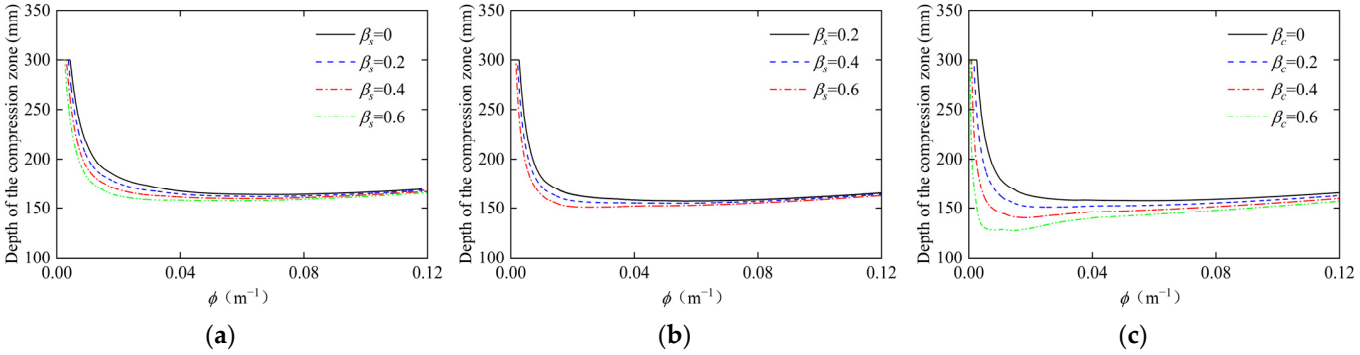


Figure 12. Variation in compression zone depth with curvature under varying preload combinations: (**a**) β_c= 0; (**b**) β_c = 0.2; (**c**) β_s = 0.6.

As demonstrated, increasing β_s and β_c promotes an earlier shift from full to partial compression in the cross-section. Moreover, both the reduction rate and magnitude of compression zone depth increase with the sectional curvature. With other conditions identical, the maximum difference in the compression zone depth reaches 32 mm between CE-CFST columns with different β_s, and 78 mm for those with different β_c, indicating that β_c has a more pronounced influence on the compression zone depth.

3.4. Effects of Two-Stage Preloads on n-P Relationship

As a fundamental parameter controlling seismic ductility in RC and composite columns, the axial compression ratio (n) is critically examined. Figure 13 provides a comparison of the n–P relationships, illustrating the variation in lateral ultimate load-bearing capacity for CE-CFST columns under various preload combinations.

The findings indicate that preload exerts a negligible effect on the critical axial compression ratio (n) corresponding to the balanced failure between large and small eccentricities in CE-CFST columns. However, the influence trend of preload on P diverges near an axial compression ratio of approximately 0.5. Specifically, when $n < 0.5$, P decreases slightly with increases in the preloads. Conversely, when $n > 0.5$, P improves to some extent with increases in the preloads. The phenomenon fundamentally stems from how preload modifies

the failure state. For a fixed axial load (i.e., a constant n), preload notably alters this depth at failure, which lowers lateral capacity under low n but has the opposite effect under high n.

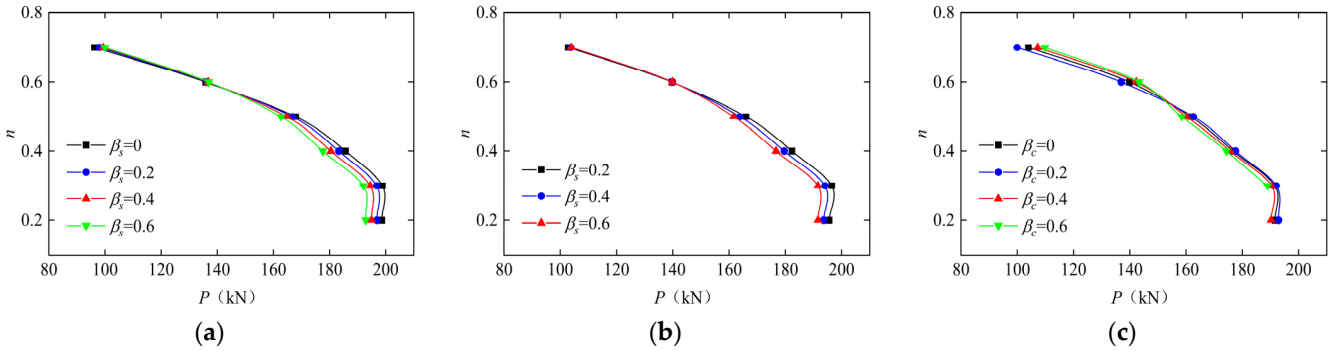


Figure 13. n–P Curves under varying preload combinations: (**a**) β_c = 0; (**b**) β_c = 0.2; (**c**) β_s = 0.6.

4. Parametric Analysis of Monotonic Compression-Bending Behavior

Existing studies have demonstrated that structural parameters—comprising the axial compression ratio (n), steel tubular diameter-to-thickness ratio (D/t), stirrup spacing (s), and encased concrete thickness (t_c)—are critical factors influencing the seismic performance of CE-CFST columns without preloads. This study employed a parametric analysis to systematically investigate the role of these parameters on how two-stage preloads affect the column's monotonic compression-bending response. In each course of each analytical process, only one of the aforementioned parameters was varied while the others were held constant. To facilitate comparative analysis, an influence coefficient for the ultimate lateral load-bearing capacity (K_p) was defined, as expressed in Equation (7).

$$K_p = \frac{P_{u0}}{P_u} \tag{7}$$

where P_{u0} and P_u represent the lateral ultimate load capacities of CE-CFST columns without and with preloads, respectively.

4.1. Effect of Axial Compression Ratio (n)

In the design of both RC and steel-concrete composite columns, the axial compression ratio (n) is a primary factor that controls the achievable lateral load-bearing capacity and ductility. This study examines its effects across a range of 0.2 to 0.7.

Figure 14 presents the relationship between K_p and the preload coefficients under different scenarios: Figure 14a shows the variation when only the steel tubular preload coefficient (β_s) is modified, while Figure 14b displays the corresponding changes for adjustments in the in-tube concrete preload coefficient (β_c). The results indicate that at axial compression ratios $n \leq 0.5$, K_p consistently decreases as the preload coefficients (β_s and β_c) increase, with maximum reductions of 3.2% and 2.5% observed, respectively. For identical preload coefficients, the absolute values of K_p under different axial compression ratios differ by up to 1.2%. Conversely, when $n > 0.5$, K_p increases with rising preload coefficients, reaching maximum increments of 1.4% and 9.9%, respectively. Under identical preload conditions, the variation in K_p across different axial compression ratios reach up to 8.1%.

These results identify the axial compression ratio (n) as a key determinant that moderates the effect of two-stage preloads on K_p. The underlying principle is that over 70% of the lateral load is consistently carried by the encased concrete throughout the monotonic compression-bending process. The presence of preloads alters the internal load distribution, reducing the actual axial compression ratio on the encased concrete. This redistribution mitigates the weakening effect of a high global axial ratio (n), thereby enhancing the ul-

timate lateral capacity. These insights lead to distinct design strategies: in regions with $n < 0.5$, the beneficial effect allows for more economical designs. In regions with $n \geq 0.5$, the preload-induced reinforcement should be leveraged and can be further enhanced by increasing the cross-sectional area or specifying a lower diameter-to-thickness ratio.

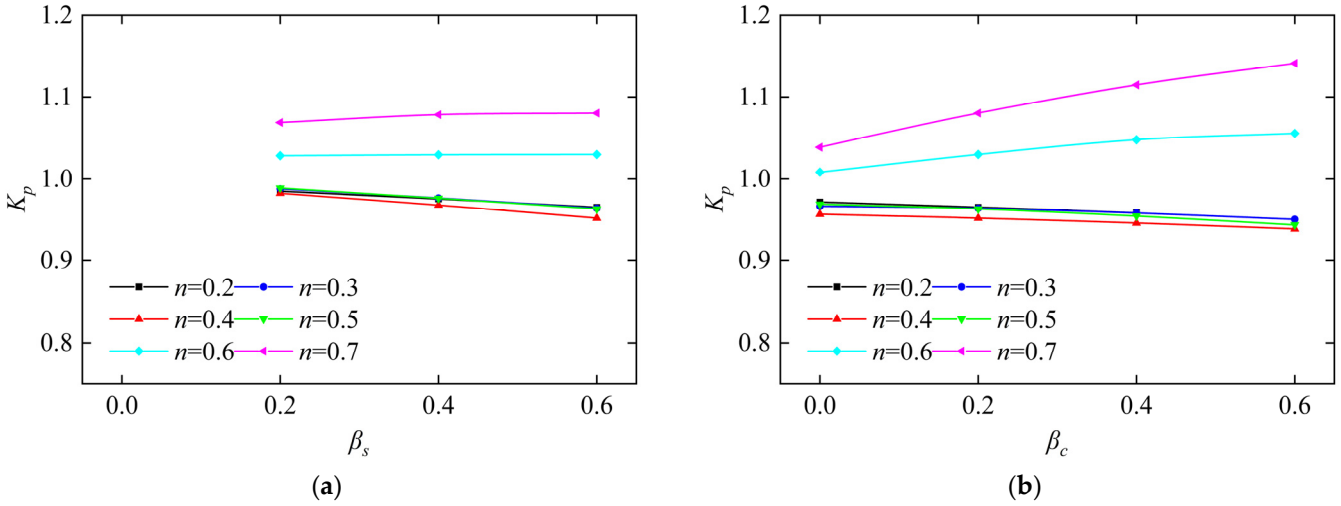


Figure 14. Influence of preload coefficients on K_p under varying axial compression ratios: (**a**) β_c = 0.2; (**b**) β_s = 0.6.

4.2. Effects of Steel Tubular Diameter-to-Thickness Ratio (D/t)

The seismic performance of both the inner CFST component and the overall column is primarily controlled by the steel tubular diameter-to-thickness ratio (D/t), as it determines the degree of confinement provided to the in-tube concrete. This ratio was investigated by varying the tube thickness to 4, 6, 8, and 10 mm.

Figure 15a,b contrast the variation of K_p with β_s when only the steel tubular preload or the in-tube concrete preload is modified, respectively. As observed in Figure 15a, for a given β_s, K_p decreases with reducing D/t ratio. At a fixed D/t ratio, the maximum and minimum reductions in K_p are 3.3% and 2.1%, respectively, resulting in a difference of 1.2%. From Figure 15b, an inverse relationship between K_p and the D/t ratio is indicated for a given β_c. At a constant D/t ratio, the reduction in K_p ranges from 1.3% to 2.1%, corresponding to a variation of 0.8%.

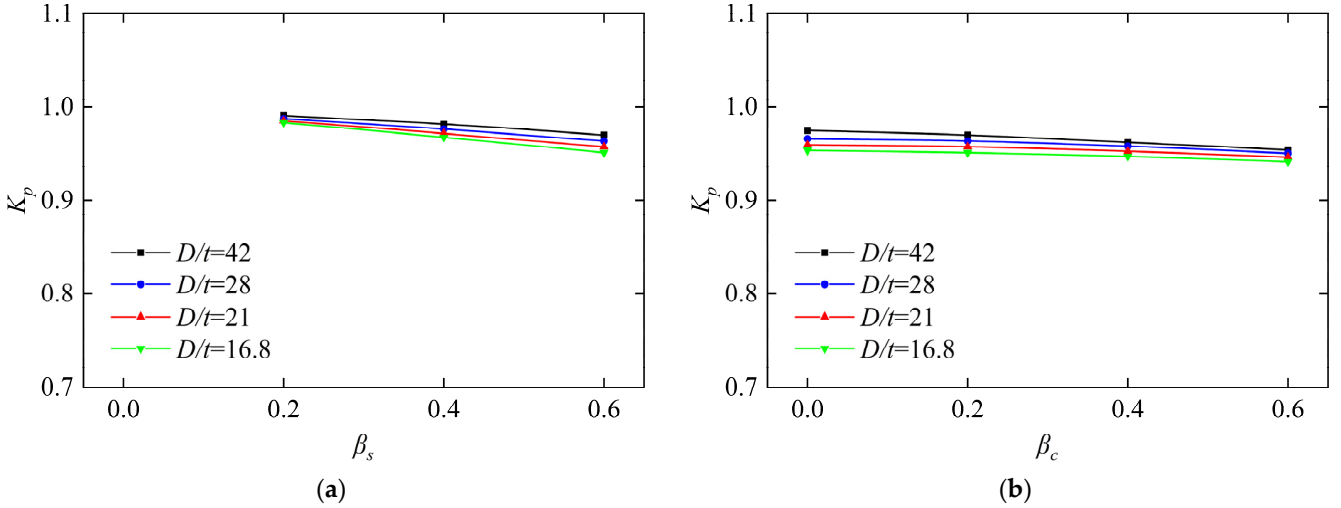


Figure 15. Influence of preload coefficients on K_p under different diameter-to-thickness ratios: (**a**) β_c = 0.2; (**b**) β_s = 0.6.

These findings confirm that the D/t ratio plays a dual role: it modifies the influence of steel tubular preload on K_p while concurrently governing the sensitivity to in-tube concrete preload. The underlying mechanism is that for a given β_s, a thicker steel tube (corresponding to a smaller D/t ratio) carries higher preload, thereby supporting a larger proportion of the axial load. This lowers the actual axial compression ratio in the encased concrete, thereby diminishing its lateral load capacity. Therefore, one should specify a maximum D/t ratio in critical regions (e.g., lower piers) to enhance stability, and permit a higher ratio in secondary areas to optimize economy.

4.3. Effects of Stirrup Spacing (s)

The stirrup ratio, a key parameter of the encased concrete's strength and ductility, was investigated by modifying the stirrup spacing. The analysis considered spacings of 40, 60, 80, and 100 mm.

Figure 16 examines the effects of preloads on K_p under different stirrup spacings, presenting results for the steel tube (Figure 16a) and the in-tube concrete (Figure 16b) separately. Figure 16a demonstrates that K_p increases with reduced stirrup spacing at a constant β_s. And at a constant stirrup spacing, K_p decreases with increasing β_s, with maximum and minimum reductions of 3.4% and 1.8%, respectively, resulting in a difference of 1.6%. From Figure 16b, for a given β_c, K_p remains largely unchanged with decreasing stirrup spacing. Under fixed stirrup spacing, K_p decreases as β_c increases, showing maximum and minimum reductions of 2.5% and 1.6%, respectively, with a difference of 0.7%. These results demonstrate that stirrup spacing governs how steel tubular preload affects K_p, while playing an insignificant role in the in-tube concrete's preload effect.

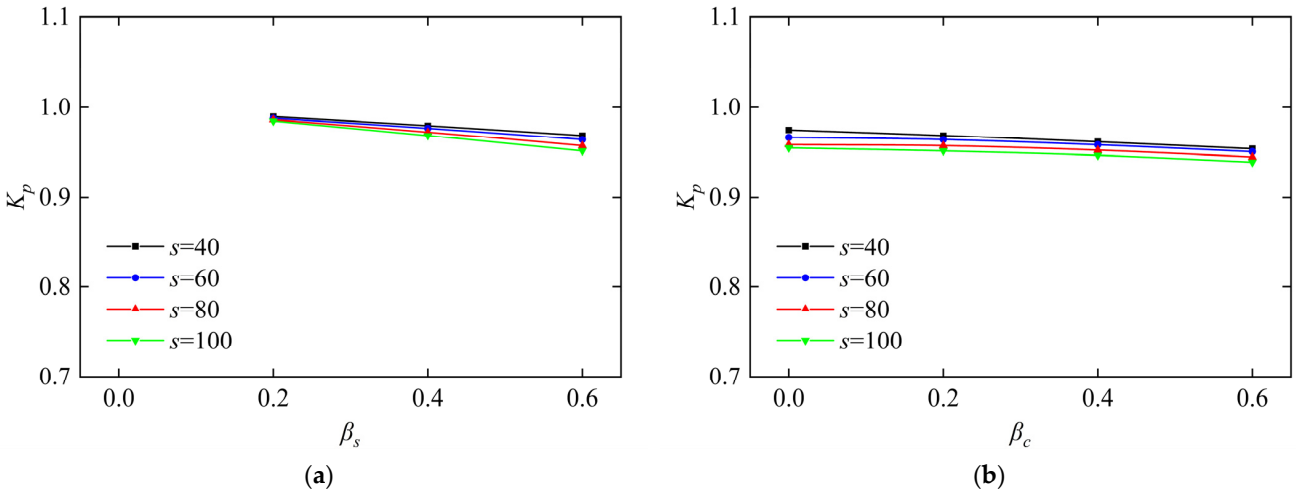


Figure 16. Influence of preload coefficients on K_p under different stirrup spacings: (**a**) β_c = 0.2; (**b**) β_s = 0.6.

4.4. Effects of Encased Concrete Thickness (t_c)

The ratio of the steel tubular diameter to the cross-sectional width was examined by varying the encased concrete thickness. The parametric study considered thicknesses of 280 mm, 300 mm, and 320 mm to quantify its influence on mechanical performance.

Figure 17a,b present the evolution of K_p with preloads in the steel tube and in-tube concrete, respectively, across different encased concrete thicknesses. This visual similarity between the two sets of curves indicates that the encased concrete thickness plays a negligible role in moderating the influence of either type of preload on K_p.

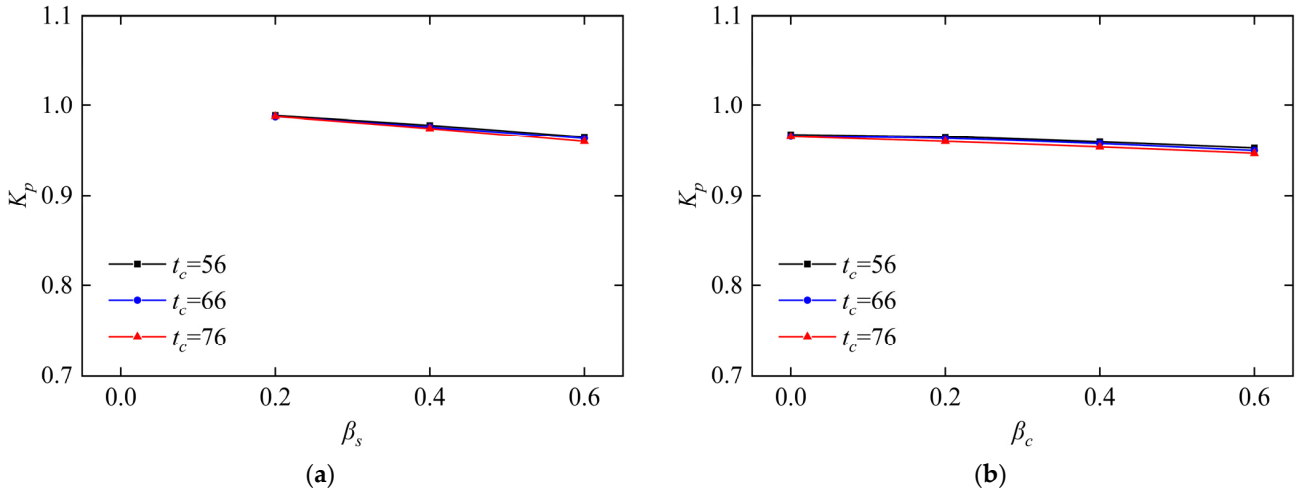


Figure 17. Influence of preload coefficients on K_p under varying encased concrete thicknesses: (**a**) β_c = 0.2; (**b**) β_s = 0.6.

The above parametric analysis reveals that the principal parameters governing the steel tubular preload effect on K_p are the axial compression ratio (n), stirrup ratio, and steel tubular diameter-to-thickness ratio (D/t). For the influence of in-tube concrete preload, the axial compression ratio (n) and the steel tubular diameter-to-thickness ratio (D/t) ratio emerge as the key factors. Consequently, these identified parameters require comprehensive consideration in both predicting the ultimate lateral-bearing capacity of CE-CFST columns with two-stage preloads and developing corresponding restoring force models.

5. Establishment of Restoring Force Model of CE-CFST Columns with Two-Stage Preloads

To comprehensively elucidate the seismic property of CE-CFST columns under two-stage preloads, in addition to assessing their monotonic compression-bending behavior, it is imperative to develop a restoring force model capable of predicting hysteretic response. This model incorporates the skeleton curve with hysteretic rules to quantify structural strength, stiffness, and degradation characteristics, thereby enabling accurate prediction of structural member behavior under cyclic seismic loading. Accordingly, this study proposes a degenerate trilinear restoring force model illustrated in Figure 18 for CE-CFST columns with two-stage preloads.

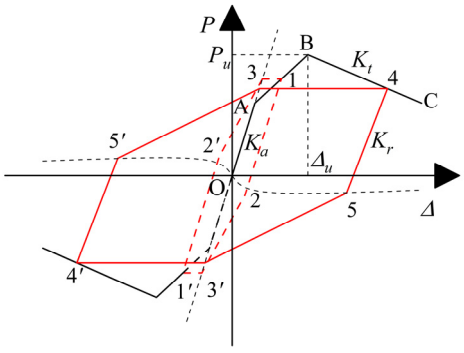


Figure 18. Degenerate trilinear restoring force model.

5.1. Establishment of Skeleton Curve

Establishing the skeleton curve is the primary step in formulating the degenerate trilinear restoring force model. This curve is defined by three critical points (A, B, and C

in Figure 18): Point A (the yield point) defines the onset of the hardening stage; Point B (the peak point) indicates the transition from the hardening to the descending stage; and Point C (the failure point) defines the termination of the skeleton curve. Consequently, the key model parameters include: yield load (P_y), elastic stiffness (K_a), ultimate lateral load-bearing capacity (P_u) and its corresponding peak displacement (Δ_u), degradation stiffness in the descending stage (K_t), failure load (P_z), and unloading stiffness (K_r).

This study employs a combined approach of curve fitting and theoretical calculation to determine these key parameters. The restoring force model for CE-CFST columns incorporating two-stage preloads was developed by integrating the identified parameters with established hysteretic rules. Theoretical calculations utilize the same constitutive models and fundamental assumptions outlined in Section 2.2, while concrete's tensile contribution is neglected to streamline the computational procedure. The selection and calculation procedures for the key parameters are detailed in the following sections. According to the parametric analysis, the parameters fall into two distinct categories: those sensitive to the two-stage preloads and those largely unaffected by them.

5.1.1. Parameters Unaffected by Two-Stage Preloads

1. Yield load

   The yield load P_y is calculated using the following formula [27]:

$$P_y = 0.6P_u \tag{8}$$

where P_u is the ultimate lateral load-bearing capacity.

2. Peak displacement

   The peak displacement (Δ_u) is predicted using the following formula [29]:

$$\phi_u = \varepsilon_{cu}/c \tag{9}$$

$$\Delta_u = \frac{1}{3}\phi_u H^2 \tag{10}$$

where $\varnothing_u$ represents the ultimate curvature corresponding to the peak load; ε_{cu} represents the ultimate compressive strain of concrete at the compression edge; and c represents the vertical distance between the neutral axis to the concrete compression edge.

3. Failure load

   The failure load (P_z) is given by the following expression [30]:

$$P_z = 0.85P_u \tag{11}$$

4. Unloading stiffness

   The unloading stiffness (K_r) is determined using the following formula [27]:

$$K_r = \begin{cases} K_a & |\Delta_r| \le \Delta_u \\ \left(\frac{\Delta_u}{\Delta_r}\right)^{\zeta} & |\Delta_r| > \Delta_u \end{cases} \tag{12}$$

where Δ_r denotes the displacement at the unloading point, and ζ is an empirical coefficient taken to be 1.2.

5.1.2. Parameters Affected by Two-Stage Preloads

1. Elastic stage stiffness

The initial elastic stiffness (K_a) for CE-CFST columns without preloads is calculated according to the pure bending member stiffness formula provided in a previous study [25] (Equation (13)). Furthermore, given that the axial compression ratio (n) negligibly impacts the flexural stiffness in the elastic stage, the elastic flexural stiffness can be accurately estimated by applying the calculation method devised for pure bending members, as given in Equation (13).

$$K_1 = 3(E_{s,s}I_s + E_{s,l}I_l + E_{c,core}I_{core} + E_{c,out}I_{out})/H^3 \quad (13)$$

where the elastic modulus and moment of inertia are defined as follows: $E_{s,s}$ and I_s for the steel tube; $E_{s,l}$ and I_l for the longitudinal reinforcement bars; $E_{c,core}$ and I_{core} for the in-tube concrete; and $E_{c,out}$ and I_{out} for the encased concrete. H represents the column height.

However, under two-stage preloads, the steel tube may yield before the lateral load reaches $0.6P_u$, leading to lower elastic stage stiffness in CE-CFST columns than predicted by Equation (14) (see Figure 9). Thus, the elastic stiffness K_a for columns under two-stage preloads is derived from calculated K_1 values through regression analysis. Regression data were obtained from the elastic stage stiffness values derived from parametric analysis results of the baseline member under various preload combinations, as presented in Section 3. The regression curve incorporates the influence of both the first-stage preload coefficient (β_1) and the second-stage preload coefficient (β_2). The specific calculation is given by the following formula:

$$K_a/K_1 = f(\beta_1) \cdot f(\beta_2) \quad (14)$$

where $f(\beta_1)$ and $f(\beta_2)$ are influence factors of the first- and second-stage preloads on elastic stage stiffness, respectively. The specific formulas for these factors are as follows:

$$f(\beta_1) = {\beta_1}^2 - 0.996\beta_1 - 0.885 \quad (15)$$

$$f(\beta_2) = -0.723{\beta_2}^2 + 0.674\beta_2 + 0.885 \quad (16)$$

2. Ultimate lateral load-bearing capacity

An accurate prediction of the ultimate lateral load capacity (P_u) in compression-bending CE-CFST columns is achieved by employing the superposition method outlined in previous studies [27,28,31–33]. This approach divides the cross-section of CE-CFST columns into two distinct components: the encased reinforced concrete (RC) element and the CFST element. The composite capacity of the CE-CFST column is determined from the separate load-bearing capacities of its individual components, with the specific calculations provided below:

$$N = N_{rc} + N_{cfst} \quad (17)$$

$$M = M_{rc} + M_{cfst} \quad (18)$$

where N_{rc} and N_{cfst} represent the axial force resisted by the encased concrete component and the CFST component, respectively. M_{rc} and M_{cfst} represent the bending moment resisted by the encased concrete component and the CFST component, respectively.

To determine the ultimate lateral load capacity (P_u) of CE-CFST columns, the established internal-external force relationship $M = PL + N\Delta$ is applied once the ultimate sectional capacity (N, M) is known.

(a) Contribution of encased RC component

Figure 19 [29] depicts the calculation model, which represents the encased concrete cross-section as an I-section and is further idealized using an equivalent rectangular stress block.

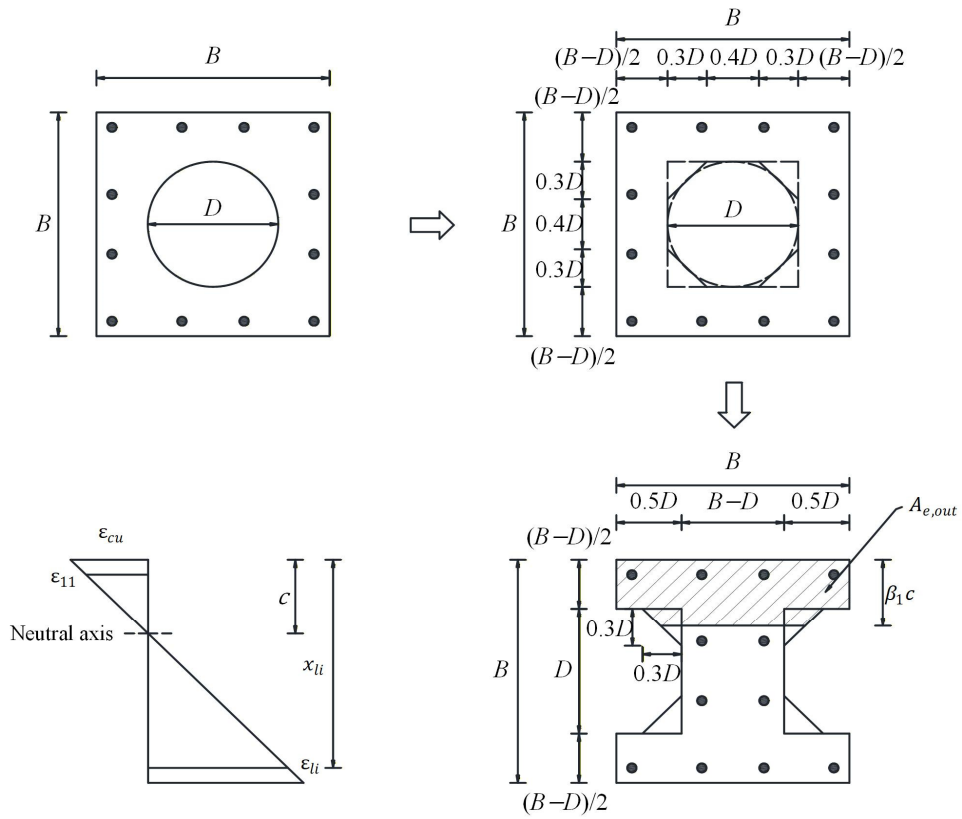


Figure 19. Simplified cross-section and strain of the encased concrete section.

Since the encased RC component is not subject to preloads, its axial force (N_{rc}) and bending moment (M_{rc}) capacities are evaluated based on established methods for conventional RC members under compression-bending [24,34]. The computational model, shown in Figure 19 [31], idealizes the cross-section as an I-section using an equivalent rectangular stress block. The capacities are then calculated based on the average compressive stress ($\alpha_1 f_{c,out}$), the equivalent compression zone height ($\beta_1 c$), and the effective area ($A_{e,out}$) of the encased concrete, as detailed in Equations (19)–(22) [24,25], where α_1 and β_1 are reduction coefficients specified in a previous study [24].

$$N_{rc} = \alpha_1 f_{c,out} A_{e,out} + \sum \sigma_{li} A_{li} \tag{19}$$

$$M_{rc} = \alpha_1 f_{c,\mathrm{out}} A_{e,\mathrm{out}} \left(\frac{B}{2} - x_{c,\mathrm{out}} \right) + \sum \sigma_{li} A_{li} \left(\frac{B}{2} - x_{li} \right) \tag{20}$$

$$\sigma_{li} = E_{s,l} \varepsilon_{cu} \frac{c - x_{li}}{c} \quad (|\sigma_{li}| \le f_l) \tag{21}$$

$$\varepsilon_{li} = \varepsilon_{cu} (c - x_{li}) / c \tag{22}$$

where $A_{e,out}$ and A_{li} represent the areas of the equivalent stress block of the encased concrete and the longitudinal reinforcement bars, respectively. $x_{c,out}$ and x_{li} represent the distances from the centroids of the encased concrete equivalent stress block and the longitudinal reinforcement to the compression edge, respectively. σ_{li} and ε_{li} represent the stress and strain in the longitudinal reinforcement.

(b) Contribution of CFST Component

The axial force and bending moment resisted by the CFST component are calculated following established methods [24,27,34]. In this model, the in-tube concrete is idealized

using an equivalent rectangular stress block (Figure 20), enabling the computation of axial force (N_{core}) and bending moment (M_{core}) through the following simplified expressions [27]:

$$N_{\text{core}} = \gamma A_{c,\text{core}} \sigma_{e,\text{core}} \tag{23}$$

$$M_{\text{core}} = \gamma A_{c,\text{core}} \sigma_{e,\text{core}} (0.5B - x_{e,\text{core}}) \tag{24}$$

where $\sigma_{e,core}$ represents the stress at the centroid of the compression zone of the in-tube concrete, $x_{e,core}$ represents the distance from the centroid of the compression zone to the compression edge, and $A_{e,core}$ is the area of the compression zone. γ is the equivalent area coefficient.

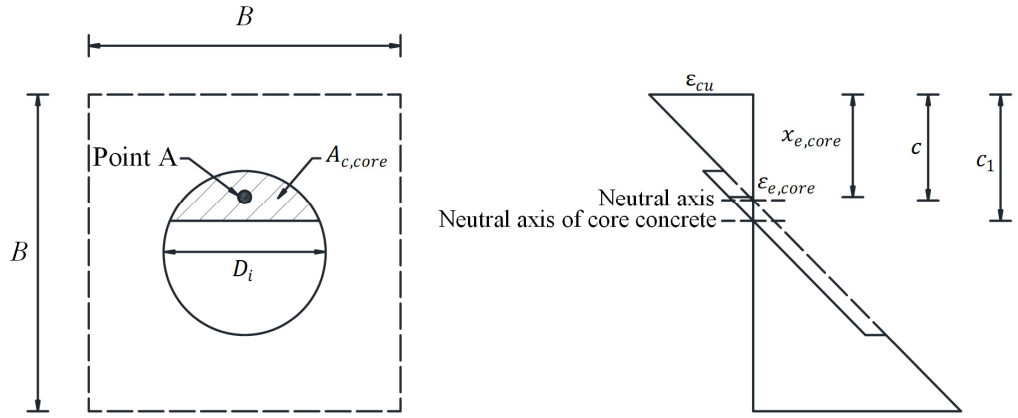


Figure 20. Strain in the in-tube concrete section.

It is important to note that the in-tube concrete is subjected to second-stage preload, which must be accounted for in the calculations. As illustrated in Figure 20, the depth of the neutral axis (c_1) determined from analyzing the CFST component in isolation differs from that of the overall composite section (c). This isolated neutral axis depth (c_1) for the CFST component is calculated using the following formula:

$$c_1 = \left(\frac{\beta_2 f_{ys}}{E_{ss} \varepsilon_{cu}} + 1 \right) c \tag{25}$$

The axial force (N_s) and bending moment (M_s) resisted by the steel tube are determined by the following simplified expressions [32]:

$$N_s = k_1 f_{ys} A_s \tag{26}$$

$$M_s = k_2 f_{ys} A_s D \tag{27}$$

Critically, the steel tube experiences combined first- and second-stage preloads, which must therefore be accounted for in the analysis. As shown in Figure 21, this results in a distinct neutral axis depth (c_2) for the steel tube alone, differing from that of the global composite section (c). This isolated neutral axis depth (c_2) for the steel tube is determined using the following expression:

$$c_2 = \left[\frac{(\beta_1 + \beta_2) f_{ys}}{E_{ss} \varepsilon_{cu}} + 1 \right] c \tag{28}$$

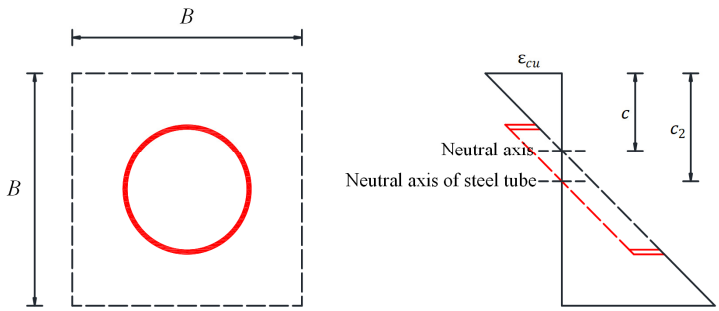


Figure 21. Strain in the steel tube section.

The relevant parameters in Equations (23)–(28) can be found in the references [27,34].

3. Degradation stiffness in descending stage

The degradation stiffness (K_t) is determined through regression analysis, utilizing data obtained from the parametric analysis of CE-CFST columns subjected to different preload conditions as presented in Section 3. The regression model incorporates the influence of multiple parameters: the first-stage preload coefficient (β_1), second-stage preload coefficient (β_2), axial compression ratio (n), stirrup ratio (ρ), and steel tubular ratio (α, defined as the steel tubular volume to the total specimen volume). The calculation is performed as follows:

$$K_t / K_a = -f(\beta_1) \cdot f(\beta_2) \cdot f(n) \cdot f(\rho) \cdot f(\alpha) \tag{29}$$

$$f(\beta_1) = 0.057\beta_1 + 0.501 \tag{30}$$

$$f(\beta_2) = 0.467\beta_2 + 1.025 \tag{31}$$

$$f(n) = 3.921n + 0.852 \tag{32}$$

$$f(\rho) = -8.662\rho + 0.854 \tag{33}$$

$$f(\alpha) = 0.691\alpha + 0.062 \tag{34}$$

5.2. Hysteretic Rules

As shown in Figure 18, the hysteretic rules for the restoring force model of CE-CFST columns under two-stage preloads can be concluded as follows:

1. Elastic stage (O–A): For loads below the yield load (P_y), both loading and unloading are collinear along segment O–A, defining the stage of constant stiffness K_a.
2. Hardening stage (A–B): When the load exceeds P_y but remains below the ultimate load P_u, the loading path follows segment A–B. Unloading from any point 1 on segment A–B is directed toward point 2, with both loading and unloading stiffnesses equal to K_a. The absolute load value at point 2 is one-fifth of that at point 1. Reloading then commences in the reverse direction from point 2 to point 3, where the absolute load value equals that at point 1. Subsequent loading continues to point 1′ on the skeleton curve. These rules are repeated analogously for forward loading, thereby completing a full hysteretic loop.
3. Descending stage (B–C): Upon exceeding the peak displacement (Δ_u) while remaining below the failure displacement (Δ_z), the loading path follows segment B–C. Unloading from any point 4 on segment B–C proceeds toward point 5 with unloading stiffness (K_r). The absolute load value at point 5 equals one-fifth of that at point 4. Reloading then continues in the reverse direction from point 5 to point 6, where the absolute load value matches that at point 4. Subsequent loading proceeds to point 4′ on the skeleton curve, and the same rules apply for forward loading, thereby completing the hysteretic loop.

4. Loop continuation: The complete restoring force model is assembled through the systematic synthesis of all hysteretic loops, each generated by the aforementioned rules, with the skeleton curve serving as the foundational backbone.

5.3. Validation of the Restoring Force Model

To validate the accuracy of the restoring force model, eight CE-CFST specimens were designed and subjected to numerical analysis. The basic parameters, including geometric dimensions and material mechanical properties, are consistent with those of the baseline member described in Section 2.1.

The investigated parameter combinations and their corresponding peak loads, as calculated by the fiber element method and the restoring force model, are detailed in Table 2. The parameters include the preload coefficients (β_1, β_2), axial compression ratio (n), stirrup ratio (ρ), and steel tubular ratio (α). Here, P_{res} is the average ultimate lateral load-bearing capacity calculated by the restoring force model in both positive and negative loading directions. The comparison yields a mean P_{res}/P_{fib} ratio of 0.98 with a standard deviation of 0.0004, indicating close agreement between the fiber element method and restoring force model. As shown in Figure 22, the hysteretic behavior from the proposed model exhibits strong consistency with the reference skeleton curves generated by the fiber element method. These results validate the rationality and accuracy of the developed restoring force model.

Table 2. Comparison of results between the restoring force model and fiber model.

Specimen	β_1	β_2	n	ρ	α	P_{fib}	P_{res}	P_{res}/P_{fib}
1	0	0	0.3	0.022	0.034	198.8	194.8	0.98
2	0.2	0.2	0.3	0.022	0.034	193.9	193.9	1.0
3	0.2	0.2	0.2	0.022	0.034	193.6	189.8	0.98
4	0.2	0.2	0.4	0.022	0.034	179.6	176.04	0.98
5	0.2	0.2	0.3	0.032	0.034	197.1	193.1	0.98
6	0.2	0.2	0.3	0.016	0.034	191.7	187.9	0.98
7	0.2	0.2	0.3	0.022	0.023	187.4	183.6	0.98
8	0.2	0.2	0.3	0.022	0.045	197.2	193.3	0.98

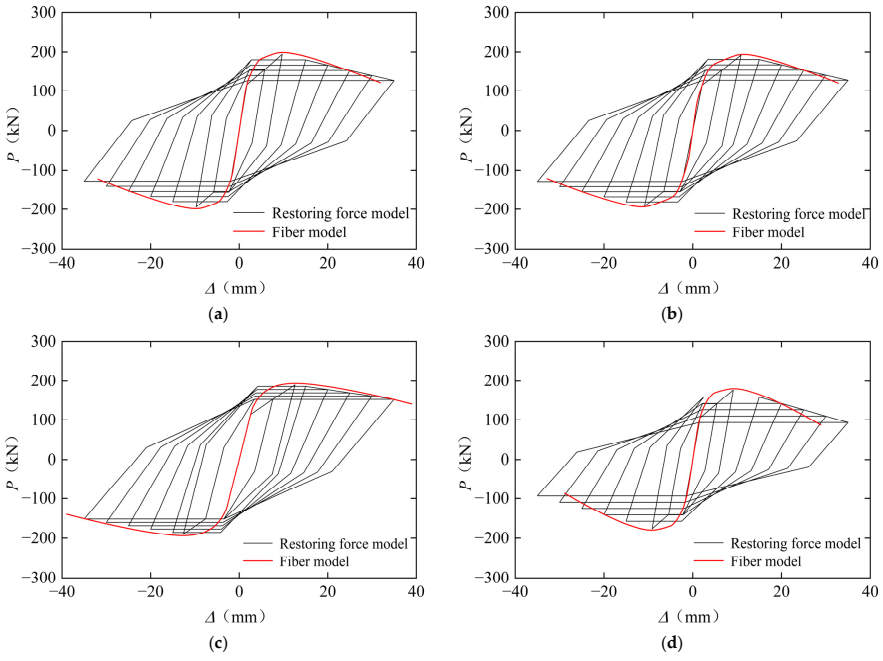


Figure 22. *Cont.*

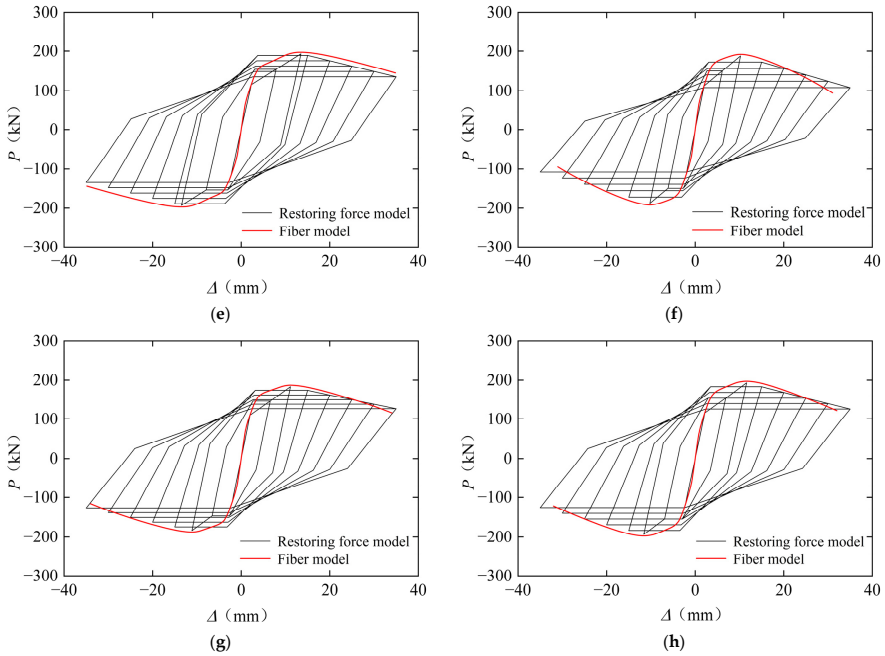


Figure 22. Comparison of the restoring force model with numerical analysis results: (**a**) Specimen 1; (**b**) Specimen 2; (**c**) Specimen 3; (**d**) Specimen 4; (**e**) Specimen 5; (**f**) Specimen 6; (**g**) Specimen 7; (**h**) Specimen 8.

6. Conclusions

Based on the research results, the following conclusions are derived:

1. Two-stage preloads significantly alter the internal force distribution by reducing the axial compression ratio (n) carried by the external reinforced concrete (RC) component and conversely increasing that borne by the internal concrete-filled steel tubular (CFST) component. This redistribution alters the relationship between the axial compression ratios of these components and their respective critical axial compression ratios. This redistribution consequently exhibits a threshold behavior around $n = 0.5$: it enhances both the lateral ultimate bearing capacity and ductility at lower ratios ($n < 0.5$) but impairs them at higher ratios ($n > 0.5$). For the baseline columns with $n = 0.3$, the ultimate lateral load-bearing capacity and its corresponding displacement were maximally improved by 3.4% and 18.9%, respectively, across the investigated preload combinations.
2. The preloads lead to a significant reduction in the compression zone depth of the CE-CFST section. Specifically, as the preloads increase, the transition from a fully compressed cross-section to a partially compressed cross-section occurs at an earlier stage. Moreover, both the rate and magnitude of the reduction in compression zone depth with increasing sectional curvature become more pronounced. The baseline columns show a maximum compression zone depth variation of 32 mm with changes in steel tubular preload, compared to 78 mm with in-tube concrete preload variation, demonstrating that the in-tube concrete preload has a significantly more pronounced effect on compression zone development.
3. Parametric analysis reveals the axial compression ratio (n), stirrup ratio (ρ), and diameter-to-thickness ratio (D/t) as dominant factors governing steel tubular preload effects. In comparison, in-tube concrete preload is primarily moderated by n and D/t ratios.
4. Following the conventional framework for curve-type restoring force models, a specialized degenerate trilinear model was established for CE-CFST columns with two-stage

preloads using parameters derived from monotonic compression-bending analysis. Consequently, it can serve as a practical sectional constitutive relationship for the seismic analysis of structures incorporating CE-CFST members with two-stage preloads.

This study provides a fiber model and a restoring force model for the monotonic compression-bending performance and seismic performance of CE-CFST columns subjected to two-stage preloads, respectively, which provides a basis for future research. In addition, the proposed restoring force model should be extended to general cyclic loading scenarios to fully capture energy dissipation and strength degradation under repeated seismic loads. These advances hope to provide reference for the seismic design of CE-CFST columns subjected to two-stage preloads.

Author Contributions: Conceptualization, B.T.; methodology, M.Z. and E.M.; software, M.Z. and E.M.; validation, M.Z. and B.T.; formal analysis, M.Z. and E.M.; investigation, M.Z. and B.T.; resources, B.T.; data curation, M.Z. and E.M.; writing—original draft preparation, M.Z. and E.M.; writing—review and editing, B.T.; visualization, M.Z.; supervision, B.T.; project administration, B.T.; funding acquisition, B.T. All authors have read and agreed to the published version of the manuscript.

Funding: This research was funded by [National Natural Science Foundation of China] grant number [52108124] and [Open Foundation of State Key Laboratory of Mountain Bridge and Tunnel Engineering, Chongqing Jiaotong University] grant number [SKLBT-2211].

Data Availability Statement: The original contributions presented in this study are included in the article. Further inquiries can be directed to the corresponding author.

Conflicts of Interest: The authors declare no conflicts of interest.

References

1. Han, L.; Tao, Z. *Modern Composite and Hybrid Structures: Experiments, Theories and Methods*; Yang, J., Ed.; Science Press: Beijing, China, 2009; pp. 1–14. (In Chinese)
2. Han, L.; Liao, F. Performance of concrete filled steel tube reinforced concrete columns subjected to cyclic bending. *J. Constr. Steel Res.* **2009**, *65*, 1607–1616. [CrossRef]
3. Xu, L.; Sun, J.G. Finite Element Analysis on the Temperature Field within Steel Tube Reinforced Columns. *Adv. Mater. Res.* **2011**, *163*, 2089–2093. [CrossRef]
4. Liao, F.; Han, L. Behaviour of composite joints with concrete encased CFST columns under cyclic loading: Experiments. *Eng. Struct.* **2014**, *59*, 745–764. [CrossRef]
5. Swaddiwudhipong, S.; Jiang, D. Steel-reinforced concrete joints under reversal cyclic load. *Mag. Concr. Res.* **2003**, *55*, 525–535. [CrossRef]
6. Han, L.; Mou, T. Design theory of CFST (concrete-filled steel tubular) mixed structures and its applications in bridge engineering. *China Civ. Eng. J.* **2020**, *53*, 1–24. (In Chinese)
7. Park, H.; Lee, H. Concrete-filled steel tube columns encased with thin precast concrete. *J. Struct. Eng.* **2015**, *141*, 4015056. [CrossRef]
8. Tu, B.; Li, Y. Axial Compressive Behavior of Concrete-Encased CFST Stub Columns with High-Level Two-Stage Initial Stresses. *J. Bridge Eng.* **2022**, *27*, 4022116. [CrossRef]
9. Chen, B.; Qin, Z.; Chen, Y. Equivalent beam-column method for simplified calculation of ultimate bearing capacity of concrete filled steel tubular arch. In Proceedings of the 16th National Bridge Academic Conference, Changsha, China, 1 May 2004. (In Chinese).
10. Wei, J.; Wu, Q. Equivalent beam-column method to estimate in-plane critical loads of parabolic fixed steel arches. *J. Bridge Eng.* **2009**, *14*, 346–354. [CrossRef]
11. Wei, J.; Chen, B. Equivalent beam-column method to calculate nonlinear critical load for cfst arch under compression and bending. *Eng. Mech.* **2010**, *2010*, 104–109. (In Chinese)
12. Lin, S.; Chen, B. Calculation of load-carrying capacity of reinforced concrete arch basing on equivalent beam-column method. *J. Fuzhou Univ. (Nat. Sci. Ed.)* **2016**, *2016*, 110–114. (In Chinese)
13. Ji, X.; Kang, H. Seismic behavior and strength capacity of steel tube-reinforced concrete composite columns. *Earthq. Eng. Struct. Dyn.* **2014**, *43*, 487–505. [CrossRef]

14. Qian, J.; Kang, H. Experimental study on seismic behavior of high-strength concrete-filled steel tube composite columns. *J. Build. Struct.* **2009**, *30*, 85–93. (In Chinese)
15. Li, H.; Wu, B. Study on seismic performance of steel tube high strength concrete composite column. *Earthq. Eng. Eng. Vib.* **1998**, *1998*, 45–53. (In Chinese)
16. Li, H.; Wang, Z. Experimental research on mechanism and seismic performance of laminated column with steel tube filled with high-strength concrete. *Earthq. Eng. Eng. Vib.* **1999**, *1999*, 27–33. (In Chinese)
17. Huang, D.; Huang, Y. Study on seismic ductility of steel tube-reinforced concrete column. *Earthq. Eng. Eng. Vib.* **2016**, *36*, 207–214. (In Chinese)
18. Huang, Y.; Huang, D. Seismic performance limit states of steel tube-reinforced concrete columns. *Earthq. Eng. Eng. Vib.* **2018**, *38*, 157–167. (In Chinese)
19. Yu, M.; Chen, K. Seismic behavior of concrete-filled circular steel tubular columns considering initial stress. *J. Build. Struct.* **2019**, *40* (Suppl. S1), 234–240. (In Chinese)
20. Cai, W.; Shi, Q. Study on restoring force model of concrete-filled circular steel tubular columns under axial reciprocating load. *Eng. Mech.* **2021**, *38*, 170–179+198. (In Chinese)
21. Ke, X.; Yang, T. Restoring force model of high-strength concrete-encased CFST composite columns. *Struct. Des. Tall Spec. Build.* **2021**, *30*, e1894. [CrossRef]
22. Wang, M.; Shen, P. Present situation of nonlinear seismic response analysis of reinforced concrete high-rise structures. *World Inf. Earthq. Eng.* **1998**, *14*, 8. (In Chinese)
23. Jiang, L.; Zheng, C. A new method for dealing with the stiffness critical point in restoring force models. *Earthq. Eng. Eng. Vib.* **2020**, *2*, 171–176. (In Chinese)
24. *GB50010-2010*; Code for Design of Concrete Structures. China Architecture & Building Press: Beijing, China, 2010; pp. 19–27. (In Chinese)
25. *CECS 188-2005*; Technical Specification for Steel Tube-Reinforced Concrete Column Structure. Standards Press of China: Beijing, China, 2005; pp. 17–26. (In Chinese)
26. Han, L. *Concrete Filled Steel Tubular Structures-Theory and Practice*, 3rd ed.; Tong, A., Ed.; Science Press: Beijing, China, 2016; pp. 67–273. (In Chinese)
27. *T/CECS 663-2020*; Technical Specification for Concrete-Encased Concrete-Filled Steel Tubular Structures. Standards Press of China: Beijing, China, 2020; pp. 12–36. (In Chinese)
28. Shen, J.; Wang, C. *Finite Element and Shell Limit Analysis of Reinforced Concrete*; Yao, M., Ed.; Tsinghua University Press: Beijing, China, 1993; pp. 36–56. (In Chinese)
29. Huang, D. Researches on Behavior of Steel Tube-Reinforced Concrete Column. Master's Thesis, Hunan University, Hunan, China, 2017. (In Chinese).
30. Ma, D.Y.; Han, L.H. Seismic performance of concrete-encased CFST piers: Analysis. *J. Bridge Eng.* **2018**, *23*, 04017119. [CrossRef]
31. An, Y. Performance and Design Method of Square Concrete-Encased CFST Members Under Combined Compression and Bending. Ph.D. Thesis, Tsinghua University, Beijing, China, 2015. (In Chinese).
32. Zhang, J.; Li, X. Cyclic behavior of steel tube-reinforced high-strength concrete composite columns with high-strength steel bars. *Eng. Struct.* **2019**, *189*, 565–579. [CrossRef]
33. Zhang, J.; Han, W. Experimental Study of Hysteretic Behavior of Damage Controllability in Steel-Tube-Reinforced High-Strength Concrete Columns. *J. Tianjin Univ. (Sci. Technol.)* **2021**, *54*, 144–153. (In Chinese)
34. An, Y.; Han, L. Behaviour of concrete-encased CFST columns under combined compression and bending. *J. Constr. Steel Res.* **2014**, *101*, 314–330. [CrossRef]

Disclaimer/Publisher's Note: The statements, opinions and data contained in all publications are solely those of the individual author(s) and contributor(s) and not of MDPI and/or the editor(s). MDPI and/or the editor(s) disclaim responsibility for any injury to people or property resulting from any ideas, methods, instructions or products referred to in the content.